Research Article | Vol. 27, No. 6 | 18 Mar 2019 | OPTICS EXPRESS 8529
Optics EXPRESS

Voltage-tunable dual-band Ge/Si photodetector operating in VIS and NIR spectral range

E. TALAMAS SIMOLA,[1] A. DE IACOVO,[2] J. FRIGERIO,[1] A. BALLABIO,[1] A. FABBRI,[3] G. ISELLA[1] AND L. COLACE[2,*]

[1]*Politecnico di Milano, Polo Territoriale di Como - L-NESS Lab, Via Anzani 42 22100 Como, Italy*
[2]*Dipartimento di Ingegneria, Università degli Studi Roma Tre, Via Vito Volterra, 62 00146 Rome, Italy*
[3]*INFN, Università degli Studi Roma Tre, Via della Vasca Navale 84, 00146 Rome, Italy*
[*]*lorenzo.colace@uniroma3.it*

Abstract: Extending and controlling the spectral range of light detectors is very appealing for several sensing and imaging applications. Here we report on a normal incidence dual band photodetector operating in the visible and near infrared with a bias tunable spectral response. The device architecture is a germanium on silicon epitaxial structure made of two back-to-back connected photodiodes. The photodetectors show a broad photoresponse extending from 390nm to 1600nm with the capability to electronically select the shorter (400-1100 nm) or the longer (1000-1600 nm) portion with a relatively low applied voltage. Devices exhibit peak VIS and NIR responsivities of 0.33 and 0.63 A/W, respectively, a low optical crosstalk (<-30dB), a wide dynamic range (>120dB) and, thanks to their low voltage operation, maximum specific detectivities of $7 \cdot 10^{11}$cmHz$^{1/2}$/W and $2 \cdot 10^{10}$cmHz$^{1/2}$/W in the VIS and NIR, respectively.

© 2019 Optical Society of America under the terms of the OSA Open Access Publishing Agreement

1. Introduction

Photodetectors are consolidated key components of most optoelectronic systems. However, fast developing applications such as optical communications, self-driving cars, virtual/augmented reality and medical diagnostics are stimulating an increasing demand for innovation towards performance improvement not only in terms of sensitivity and speed but also of spectral response. In this framework, the near infrared (NIR) spectral range (between 780 and 2500nm) emerged as a very interesting band for several applications including (besides optical fiber communications), enhanced imaging, security, remote sensing and metrology in several fields such as food inspection, agriculture, pharmaceutical and biology [1,2].

While the market of NIR photodetectors is largely dominated by III-V semiconductor compounds (InGaAs, InGaAsP), the past two decades have seen a fast progress of germanium on silicon (Ge/Si) photodiodes. Ge, with its direct energy gap at 0.8eV, can effectively absorb optical radiation above 1600nm [3]. In addition, its compatibility with silicon promoted significant research efforts towards NIR optoelectronics integrated circuits able to combine optics and electronics functions to improve compactness, reliability and scalability while reducing the overall cost [4]. Such development was triggered by the ability to obtain high quality Ge epitaxially grown on Si, despite their relatively large (4%) lattice mismatch [5]. High performance Ge/Si detectors (comparable to their III-V counterpart) have been fabricated in both free-space [6,7] and waveguide integrated schemes [8,9] and even integrated on silicon photonics platforms [10]. Notably, in the past few years, significant progress has been made in the growth of high quality Ge epilayers, resorting to low thermal budget deposition techniques as viable approaches to CMOS compatibility [11,12] and Ge

#355627 https://doi.org/10.1364/OE.27.008529
Journal © 2019 Received 20 Dec 2018; revised 29 Jan 2019; accepted 31 Jan 2019; published 8 Mar 2019

based optoelectronic circuits monolithically integrated with silicon electronics have been successfully demonstrated [13,14].

In this work we propose to exploit the Ge/Si technology combining the Ge and Si optical properties in order to obtain dual band photodetectors to allow sensitivity in both the visible and the near infrared. While two-color detectors for the mid and far infrared already reached a remarkable development [15], very few results have been reported concerning VIS-NIR devices. These include InGaAsSb/GaSb multilayers operating between 1 and 2μm [16], InGaP/InGaAs stacked double diodes with independent operation in the 400-700nm and 700-1000nm bands, respectively [17], an InGaP/InGaAs/Ge three-color in the 400-1100nm band with optical biasing [18]. To date, only two attempts of VIS-NIR tunable photodetectors based on SiGe have been reported [19,20].

Here, we propose a novel approach that combines the optical properties of Si and high quality Ge epitaxial layers with a back-to-back device architecture to demonstrate a voltage tunable monolithically integrated photodetector operating in the VIS and NIR in the 400 to 1600nm spectral range and capable of electronically switch the spectral sensitivity between the VIS and the NIR band with a very low optical cross-talk.

2. Principle of operation

The proposed device is based on a surface-illuminated couple of back-to–back connected photodiodes made of two semiconductors sensitive to different spectral bands. The principle underlying the voltage tunable dual band operation is quite simple and relies on the combination of two effects: the spectral splitting operated by the different optical absorption of the two semiconductors and the bias dependent photoresponse of the photodiodes.

Figure 1(a) schematically shows two stacked semiconductor materials with different electronic band gap E_{g1} and E_{g2}, with $E_{g1} > E_{g2}$. The larger gap semiconductor faces the incident light beam, therefore absorbing the optical radiation at energies $h\nu$ above E_{g1} and acting as an optical filter for the second layer, which absorbs the lower energy components ($E_{g1}>h\nu>E_{g2}$). In such a structure, light can be selectively detected similarly to a multi-junction solar cell where the shorter cutoff detector (PD_1) acts as a long wavelength pass filter for the underlying longer cutoff detector (PD_2). The spectral, responses are schematically depicted in Fig. 1(b), where the corresponding cutoff wavelengths λ_1 and λ_2 are indicated. If the two photodiodes are back-to-back connected (as shown in Fig. 1(c)), when the applied voltage V_B is positive the detector PD_1 is reverse biased and the detector PD_2 is forward biased. The device detects the shorter wavelength photocurrent from PD_1, since the longer wavelength photocurrent is shunted by the low impedance of the forward biased photodiode PD_2. Similarly, when the bias polarity is reversed, only the longer wavelength photocurrent is detected. Therefore, the electrically driven dual band operation shown in Fig. 1(d) can be accomplished in a straightforward way by simply switching the polarity of the bias voltage.

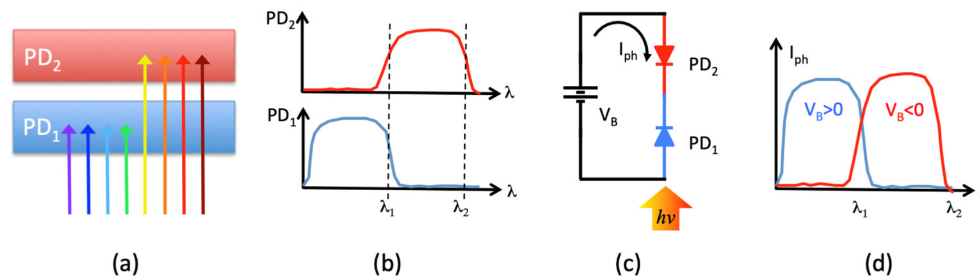

Fig. 1. Schematic representation of the principle of operation the back-to-back photodetector.

This approach has been originally proposed for WDM optical communication to simultaneously detect and demultiplex two wavelengths, avoiding additional optical

components. The double structure was fabricated using two different quaternary InGaAsP layers lattice matched to InP operating in the 0.9-1.3μm range and the voltage-controlled band selection was successfully demonstrated [21]. Modified device architectures were later proposed, based on the combination of heteroepitaxy with a back-to-back diode design to allow monolithically integrated vertically aligned detectors to operate simultaneously in the visible and near infrared [17] or to obtain wavelength sensitive photodetectors [22]. Variations of the original double diode architecture were implemented resorting to HgCdTe to move towards the mid- and long-wavelength infrared [23,24]. Following the first successful demonstrations and pushed by its relevance for security and military applications, the detectors technology based on stacked semiconductors attracted a lot of interest and dual- and three-band infrared focal plane arrays have been demonstrated [15].

In this work we propose and demonstrate for the first time a voltage tunable dual-band device based on the back-to-back photodiode architecture operating in the visible and near infrared, fabricated by epitaxial Ge-on-Si. The device structure is illustrated in the next section along with its fabrication details.

3. Fabrication

The proposed device architecture is a *pinip* stack, where the top *p* and *i* layers are made of Ge while the *nip* is Si. The epitaxial structure has been realized on a Si (001) substrate with a resistivity higher than 1000 Ω·cm and a thickness of 300 µm. A *p*-type layer has been formed on the backside of the wafer by spin-on-dopant (SOD). The boron-based SOD (PBF1.4AS Filmtronic) has been deposited on the surface by spin-coating (3000 rpm, 60s) and then soft-baked at 200°C for 120 s. The diffusion step has been performed by heating the wafer at 1100°C for 60s, thus realizing a boron-doped layer with an average concentration of $2\cdot10^{19}$ cm^{-3} and a thickness of 300 nm. Before the growth, the native oxide has been removed by soaking the wafer in aqueous hydrofluoric acid solution ($HF:H_2O$ 1:10) for 10 s.

The growth has been performed by low-energy plasma-enhanced chemical vapor deposition (LEPECVD) [25]. The first layer consists in a 200 nm thick phosphorous-doped Si layer, deposited at 760°C at a rate of 4 nm/s with a SiH_4 flux of 20 sccm. A doping concentration of $1x10^{19}$ cm^{-3} has been obtained by adding PH_3 during the growth. The second layer consists of 3 µm nominally undoped Ge, grown at 500°C, at a rate of 4 nm/s with a GeH_4 flux of 20 sccm. The typical background doping in this layer is p-type with an approximate concentration of 5×10^{15} cm^{-3} as evaluated by Hall effect and hot-point probe measurements. Six thermal annealing cycles (TAC) between 600 and 780°C, 2 minutes each, have been performed *in situ* to decrease the threading dislocation density. The final step consists in the deposition of 150 nm of boron-doped Ge, grown at 500°C, at a rate of 1 nm/s with a GeH_4 flux of 20 sccm. A p-doping density of $5\cdot10^{18}$ cm^{-3} has been obtained by adding B_2H_6 during the growth. Figure 2 shows a schematic of the sample. The band diagram, calculated with NextNano [26] assuming a natural valence band offset of ≈0.8 eV [27] and full relaxation of the Ge layer is reported in Fig. 3.

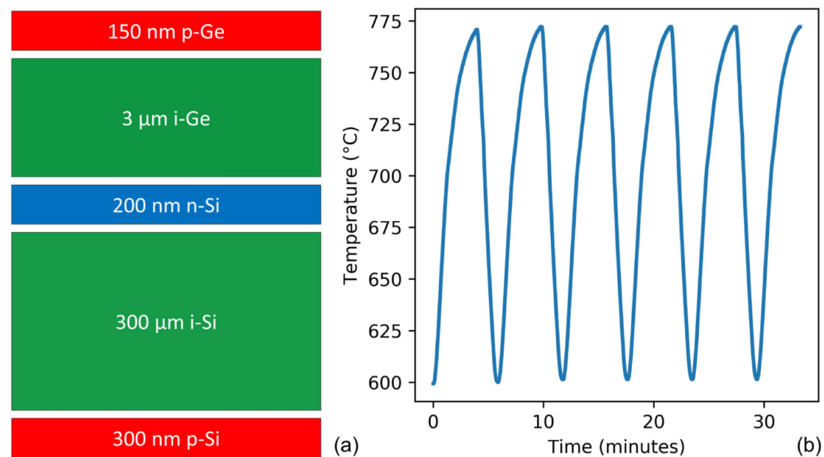

Fig. 2. (a) Schematic representation of the epitaxial stack. (b) Temperature profile during the post-growth thermal cycling.

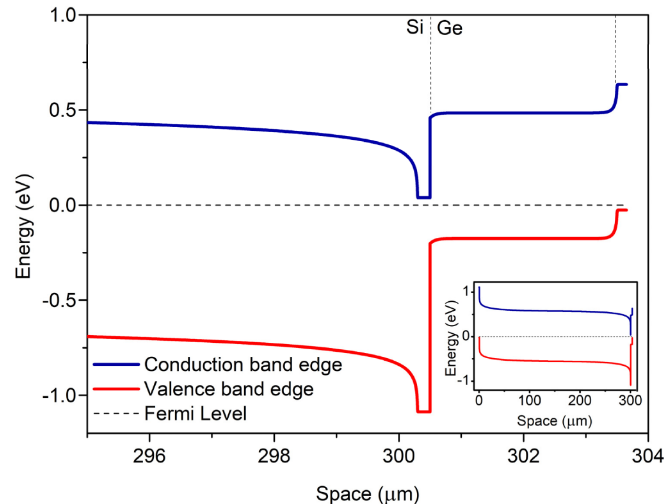

Fig. 3. Band diagram of the sample in the region around the interface between silicon and germanium. The inset shows the band diagram of the full structure.

After the growth circular mesas with diameters ranging between 100 and 500 µm have been realized by standard UV lithography and dry etching. The structure has been etched down to the intrinsic silicon to electrically isolate the different devices on the same chip. The top ohmic contacts have been realized by e-beam deposition of a Ti/Al metal stack (100 nm Ti and 1000 nm Al) and lift-off. This metal contact is also present on the n-type Si layer for preliminary tests, enabling the measurement the characteristics of the Ge *pin* and the Si *pin* independently. This intermediate contact (see Fig. 4) has been left floating during the electrical and optical measurements reported in the next sections. The bottom ohmic contact has been fabricated by depositing two rectangular stripes of Ti/Au (10 nm Ti, 150 nm of Au) on the backside of the sample. SEM images of one of the processed devices are reported in Figs. 4(a) and 4(b).

Optics EXPRESS

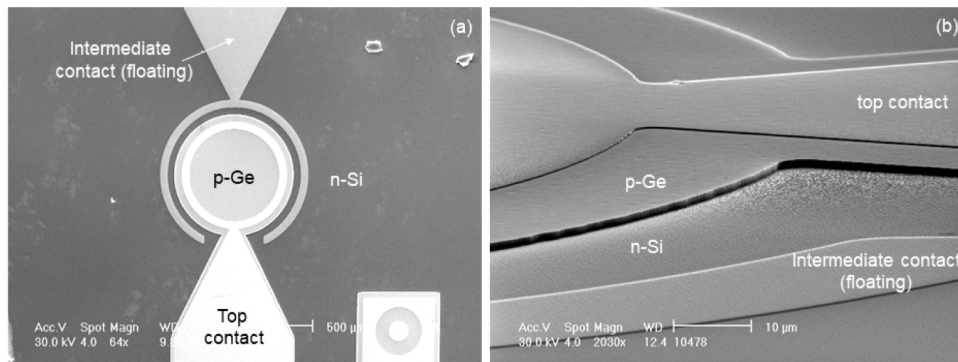

Fig. 4. SEM images of one of the processed devices in top view (a) and side view (b).

4. Results and discussion

4.1 Material characterization

The as-grown Ge-on-Si epilayer has been characterized by means of atomic force microscopy (AFM) and high-resolution X-ray diffraction (HR-XRD). An AFM scan of the sample surface is reported in Fig. 5. The RMS roughness is 0.7 nm and the threading dislocation density, evaluated by defect etching on a similar samples is $\approx 8 \times 10^6$ cm^{-2} [28].

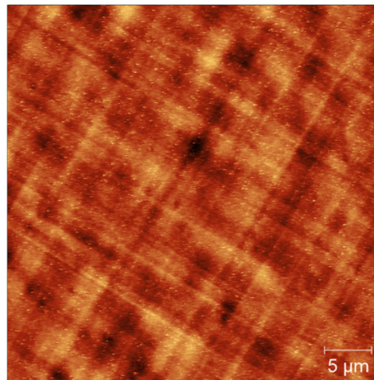

Fig. 5. 40x40 µm^2 scan of the surface of the sample.

The reciprocal space maps (RSM) relative to the symmetric (004) and asymmetric (224) reflections have been measured at grazing incidence, by a PANalytical X'Pert PRO MRD diffractometer and are reported in Fig. 6.

Out-of-plane and in-plane lattice parameters, as well as the strain state have been measured (relative to the Si reflection) for the Ge peak. Ge-on-Si typically exhibits a residual tensile strain [29], induced by the thermal expansion coefficient mismatch between Ge and Si developing during cool-down from the growth (or annealing) temperature to room-temperature. In this sample, we have measured a tensile strain of 0.17% for the Ge layer. In the RSMs, two clear peaks relative to the Si and Ge layers are present. The elongation of the Ge peak in the $q_{||}$ direction (see Fig. 6(a)) is due to the presence of defects, while the elongation toward the Si peak reveals an interdiffusion between the two materials [30,31]. The interdiffusion takes place mainly during the high temperature steps of the TAC. Relying on the interdiffusion coefficient reported in Ref [32]. we have estimated the thickness of the interdiffused region to be approximately 60 nm after the six annealing cycles shown in Fig. 2(b), therefore we do not expect any sizable effect of intermixing on the optoelectronic properties of the devices under investigation.

Optics EXPRESS

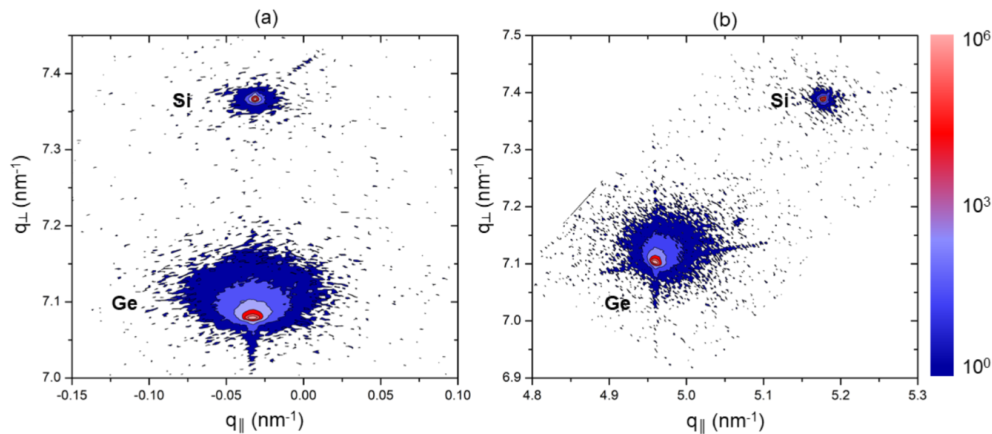

Fig. 6. RSMs for the 004 (a) and 224 (b) reflections. The color scale represents the intensity measured as counts per seconds.

4.2 Device characterization

In this section, we report and discuss the electrical and optoelectronic device characterization. Electrical measurements have been performed by a KEITHLEY 2636B source measure unit and a HP 4192A Impedance analyzer.

A typical current-voltage characteristic is shown in Fig. 7(a). The applied voltage and the measured total current are between the top *p*-contact of Ge and the bottom *p*-contact of Si, as shown in the inset. As expected from a back-to-back connected pair of diodes, the *I-V* characteristic shows two reverse currents for both bias polarities. A positive applied voltage ($V_B > 0$) forward biases the top Ge diode while reverse biasing the bottom Si diode and the total current is limited by the Si diode reverse current. When a negative voltage ($V_B < 0$) is applied, the situation is reversed. Therefore, the total current is always limited by a reverse diode current. The characteristic is not symmetrical. The Ge photodiode dark current is larger with respect to Si because of its much lower fundamental energy gap ($E_g^{Ge} = 0.66$eV, $E_g^{Si} =$ 1.12eV). In addition, the Ge photodiode, being fabricated by heteroepitaxy of mismatched semiconductors, suffers reduced crystal quality due to residual threading dislocations that negatively affect the leakage current. The typical dark current densities measured at −1V and + 1V of the Ge and Si photodiodes are 3.2mA/cm^2 and 1.6μA/cm^2, respectively. The Ge dark current density is comparable with the best reported Ge/Si photodetector technologies [33,34], demonstrating the good crystal quality of the Ge epilayer and its suitability for practical applications [35].

Figure 7(b) shows a typical capacitance voltage characteristic. The observed non-monotonic behavior is consistent with the back-to-back connected couple of diodes. A junction capacitance decreases with the reverse bias. In this double structure, it results from two series connected junction capacitances and decreases for both polarities since the Ge diode is reverse biased at negative voltages while the Si diode is reverse biased at positive voltages. The measured device capacitance is 120pF and 60pF at V_B = 1V and V_B = −1V, respectively. Such capacitances, assuming the device speed is *RC* limited and assuming the device series resistance is negligible with respect to the typical 50Ω input impedance of the analog front-end, produce estimated cutoff frequencies of about 25MHz and 50MHz, respectively.

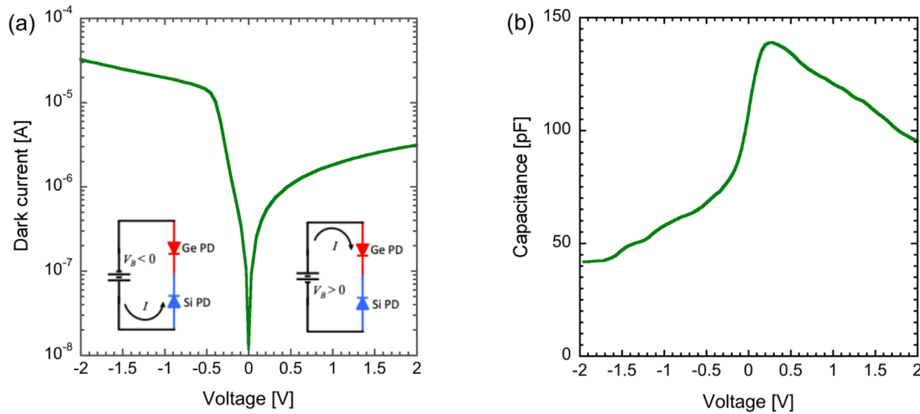

Fig. 7. (a) Current-voltage characteristic, (b) capacitance-voltage characteristic of the back-to-back photodiode.

The optical characterization was performed using a scanning monochromator equipped with a tungsten lamp and suitable filters. The optical beam is collimated and the optical power on the photodetector is measured by a calibrated power meter taking into account the two dimensional overlap between the measured beam profile and the device area. For the measurement of the dynamic range two CW fiber coupled semiconductor lasers at 633nm and 1520nm have been employed and the power was changed using a combination of neutral filters and drive current. The optical beams were coupled in air and collimated.

The bias dependent dual-band operation of the device is demonstrated in Fig. 8(a), where the spectral responsivity is shown for two different applied voltages. The operating optical bands of the two photodiodes are clearly visible. For V_B = + 1V, the Si *pin* photodiode is reverse biased and produces a photoresponse in the 400-1200nm spectral range, while the contribution from the top Ge photodiode is shunted by its high forward conductivity. The NIR-enhanced spectral response of the silicon diode is due to the quite thick active layer (about 300µm). When the bias voltage is switched to V_B = −1V, the Ge *pin* photodiode is reverse biased and produces a photoresponse in the 1000-1650nm spectral range. Its short wavelength cutoff is due to the absorption of Si. The measured peak responsivities of the two bands are 0.41A/W and 0.63A/W at 960nm and 1520nm, respectively. The spectral responses exhibit a crossover (wavelength where the two photodiodes produce the same photocurrent) at λ_c = 1080nm. The crossover wavelength depends on the amount of light absorbed by the optical filtering action of the Si diode and can be blue-shifted reducing the Si intrinsic layer thickness. The spectral response shows a region where the signals from the two diodes overlap. The amount of overlap is a measure of the crosstalk between the two wavelength bands. Such crosstalk has been defined according to:

$$C_{V_1}^{V_2}(\lambda) = 20\log\frac{I_{ph}(\lambda, V_2)}{I_{ph}(\lambda, V_1)} \quad (1)$$

where $I_{ph}(\lambda, V_i)$ is the photocurrent measured at $V_B = V_i$.

The crosstalk is reported in Fig. 8(b). In most of both bands, it is lower than –40dB and it reach 0dB (worst case) at the crossover wavelength λ_c. The device exhibits a relatively narrow overlap band (about 80nm), defined as the spectral range where the crosstalk is larger than −10dB.

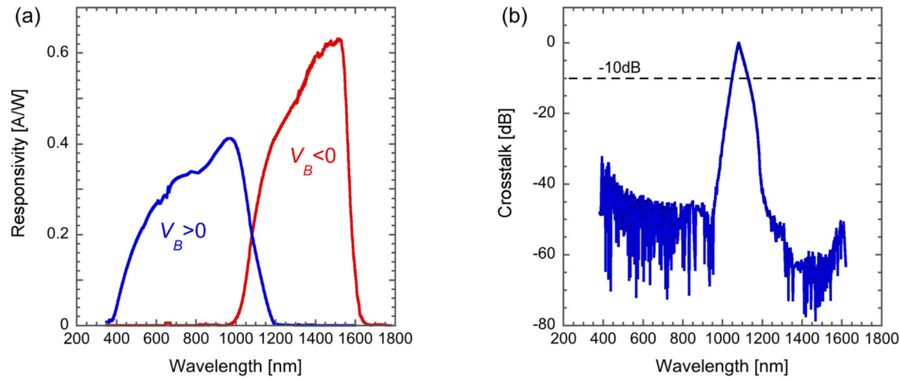

Fig. 8. (a) Device spectral responses measured at V_B = + 1V (blue) and at V_B = −1V (red), (b) wavelength crosstalk defined according to Eq. (1).

The voltage selection of the operating band can also be investigated by observing the responsivity at a constant wavelength versus the applied voltage. Figure 9(a) shows two photoresponses measured at λ = 600nm and λ = 1400nm. The VIS radiation is detected only when $V_B > -0.4$V, while the NIR is detected only for $V_B < 0$V. A crossover voltage (where the two photodiodes produce the same photocurrent) is observed at about V_c = –0.2V. The 600 and 1400nm responsivities reach their maximum values at V_B < + 1V and V_B = –0.5V, respectively. The characteristics shown in Fig. 9(a) do not significantly change with the selected wavelengths. Even in this analysis, a voltage range where the signal from the two photodiodes overlap can be observed. In this case, in order to evaluate the overlap, we have measured the voltage crossover, shown in Fig. 9(b), defined as:

$$C_{\lambda_1}^{\lambda_2}(V) = 20\log\frac{I_{ph}(V,\lambda_2)}{I_{ph}(V,\lambda_1)} \tag{2}$$

where $I_{ph}(V,\lambda_i)$ is the photocurrent measured at $\lambda = \lambda_i$.

In most of the voltage span, the device exhibits a crosstalk lower than –40dB An overlap region, defined as the voltage range where the crosstalk is larger than –10dB, is centered at V_C and spans about 100mV. Both the required bias to reach the maximum signal and the bias required to reach a given crosstalk are relevant device parameters. Indeed, the required bias should be kept low, as increasing the dark current will also affect the noise performance.

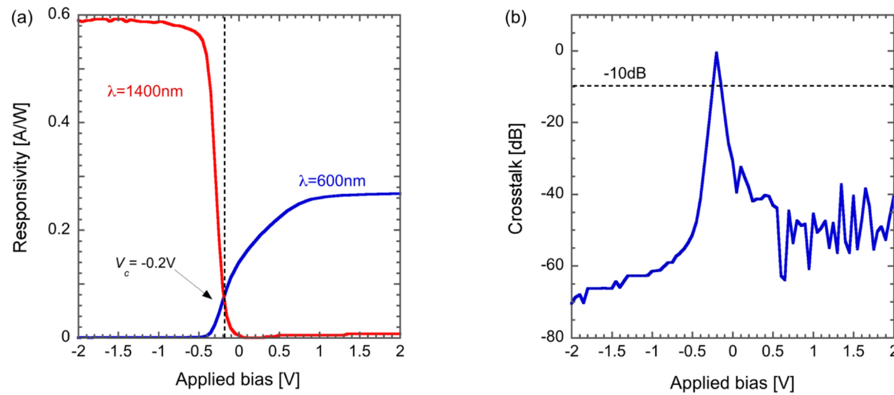

Fig. 9. (a) Photocurrent-voltage characteristics measured at optical radiation at λ = 600 (blue) and λ = 1400nm (red), (b) voltage crosstalk defined according to Eq. (2).

The overall performance of a photodetector has been evaluated by the specific detectivity D^*, defined as:

$$D^* = \frac{R\sqrt{AB}}{i_n} \tag{3}$$

where R is the responsivity, A is the device area, B is the bandwidth and i_n is the noise current. Assuming the noise current is dominated by the shot noise, i_n can be evaluated as $(2qI_dB)^{-1/2}$, where q is the electron charge and I_d is the dark current.

The resulting specific VIS (blue) and NIR (red) detectivities versus wavelength are reported in Fig. 10(a) for $V_B = +\,1V$ and $V_B = -0.5V$, respectively.

In most of the VIS spectral range, D^* is larger than 10^{11} cm√Hz/W with a peak value of $7{\cdot}10^{11}$ cm√Hz/W. In most of the NIR portion, D^* is larger than 10^{10} cm√Hz/W with a peak value of $2{\cdot}10^{10}$ cm√Hz/W. Despite its larger responsivity, the Ge photodetector exhibits a lower detectivity because of its larger dark current. An improvement of D^* could be achieved by lowering the bias voltage required to operate the device in the NIR band, thus reducing the dark current exponentially.

Finally, the linearity of the detector has been investigated at two characteristic wavelengths (630nm and 1500nm), measuring the photocurrent versus optical intensity with the device operated at $V_B = +\,1V$ and $V_B = -0.5V$, respectively. The results shown in Fig. 10(b) demonstrate a suitable linearity over several decades for both bands. A linear dynamic range, defined as the range over which photocurrent increases linearly with increasing optical power, of 124dB and 134dB has been measured for $\lambda = 633$nm and $\lambda = 1520$nm, respectively.

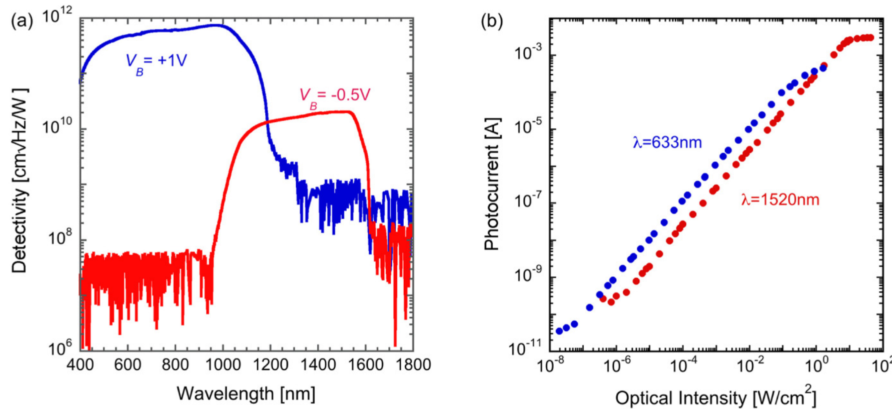

Fig. 10. (a) Specific detectivity measured at $V_B = +\,1V$ (blue) and at $V_B = -0.5V$ (red), (b) photocurrent versus optical intensity at $\lambda = 633$nm and $\lambda = 1520$nm.

5. Conclusions

In conclusion, a voltage-tunable dual-band photodetector operating in the visible and in the near infrared range has been fabricated and characterized. The device is based on a back-to-back connected couple of *pin* photodiodes made of silicon and an high quality epitaxially grown Ge layer. The device operates between 400 and 1600nm and its architecture enables to electronically select the shorter (400-1100nm) or the longer (1000-1600) portion with a relatively low applied voltage. Devices exhibit peak VIS and NIR responsivities of 0.33 and 0.63 A/W, respectively, a low optical crosstalk (<-30dB), a linear dynamic range exceeding 120dB and, thanks to their low voltage operation, maximum specific detectivities of $7{\cdot}10^{11}$cmHz$^{1/2}$/W and $2{\cdot}10^{10}$cmHz$^{1/2}$/W in the VIS and NIR, respectively. The photodetector performance demonstrates the validity of the approach and its suitability for practical

Optics EXPRESS

applications. In addition, its relatively simple two-terminal architecture and its low voltage operation suggests a broader applicability of the proposed approach for the fabrication of VIS-NIR focal plane arrays.

Funding

SEGREDIFESA of the Italian Ministry of Defence under the National Military Research Plan R&T Project (a2013.102); TEINVEIN project, POR FESR 2014-2020 (ID: 242092); EU Horizon 2020 FET project microSPIRE (ID: 766955).

Acknowledgments

The Authors would like to acknowledge the Acoustoelectronics Laboratory (ACULAB) of the Università degli Studi Roma Tre for device packaging and Fulvio Mancarella - IMM CNR for the spin-on-dopant processing.

References

1. W. H. Siesler, Near infrared spectroscopy: principles, instruments, applications, ed. By W.H. Sesler, Y. Ozaky, S. Kawata, H. M. Heise, Wiley-VCH (2006).
2. C. A. Teixeira dos Santos, R. N. P'ascoa, M. Lopo, and J. A. Lopes, "Applications of Portable Near-infrared Spectrometers," Encyclopedia of Analytical Chemistry, John Wiley & Sons, Ltd. 1–27 (2015).
3. V. Sorianello, A. Perna, L. Colace, G. Assanto, H. C. Luan, and L. C. Kimerling, "Near infrared absorption of germanium thin films on silicon," Appl. Phys. Lett. **93**(11), 111115 (2008).
4. V. A. Vu, D. E. Ioannou, R. Kamocsai, S. L. Hyland, A. Pomerene, and D. Carothers, "PIN Germanium Photodetector Fabrication Issues and Manufacturability," IEEE Trans. Semicond. Manuf. **23**(3), 411–418 (2010).
5. H. C. Luan, D. R. Lim, K. K. Lee, K. M. Chen, J. G. Sandland, K. Wada, and L. C. Kimerling, "High-quality Ge epilayers on Si with low threading-dislocation densities," Appl. Phys. Lett. **75**(19), 2909–2911 (1999).
6. Y. Kang, H. Liu, M. Morse, M. J. Paniccia, M. Zadka, S. Litski, G. Sarid, A. Pauchard, Y. Kuo, H. Chen, W. S. Zaoui, J. E. Bowers, A. Beling, D. C. McIntosh, X. Zheng, and J. C. Campbell, "Monolithic germanium/silicon avalanche photodiodes with 340 GHz gain–bandwidth product," Nat. Photonics **3**(1), 59–63 (2009).
7. I. G. Kim, K. S. Jang, J. Joo, S. Kim, S. Kim, K. S. Choi, J. H. Oh, S. A. Kim, and G. Kim, "High-performance photoreceivers based on vertical-illumination type Ge-on-Si photodetectors operating up to 43 Gb/s at λ~1550nm," Opt. Express **21**(25), 30716–30725 (2013).
8. L. Chen and M. Lipson, "Ultra-low capacitance and high speed germanium photodetectors on silicon," Opt. Express **17**(10), 7901–7906 (2009).
9. L. Vivien, A. Polzer, D. Marris-Morini, J. Osmond, J. M. Hartmann, P. Crozat, E. Cassan, C. Kopp, H. Zimmermann, and J. M. Fédéli, "Zero-bias 40Gbit/s germanium waveguide photodetector on silicon," Opt. Express **20**(2), 1096–1101 (2012).
10. D. Marris-Morini, L. Virot, C. Baudot, J. M. Fédéli, G. Rasigade, D. Perez-Galacho, J. M. Hartmann, S. Olivier, P. Brindel, P. Crozat, F. Bœuf, and L. Vivien, "A 40 Gbit/s optical link on a 300-mm silicon platform," Opt. Express **22**(6), 6674–6679 (2014).
11. M. Beals, J. Michel, J. F. Liu, D. H. Ahn, D. Sparacin, R. Sun, C. Y. Hong, L. C. Kimerling, A. Pomerene, D. Carothers, J. Beattie, A. Kopa, A. Apsel, M. S. Rasras, D. M. Gill, S. S. Patel, K. Y. Tu, Y. K. Chen, and A. E. White, "Process flow innovations for photonic device integration in CMOS," Proc. SPIE **6898**, 689804 (2008).
12. G. Dushaq, A. Nayfeh, and M. Rasras, "Metal-germanium-metal photodetector grown on silicon using low temperature RF-PECVD," Opt. Express **25**(25), 32110–32119 (2017).
13. G. Masini, V. Cencelli, L. Colace, F. Denotaristefani, and G. Assanto, "Linear array of Si-Ge heterojunction photodetectors monolithically integrated with silicon CMOS readout electronics," IEEE J. Sel. Top. Quantum Electron. **10**(4), 811–815 (2004).
14. R. Kaufmann, G. Isella, A. Sanchez-Amores, S. Neukom, A. Neels, L. Neumann, A. Brenzikofer, A. Dommann, C. Urban, and H. von Känel, "Near infrared image sensor with integrated germanium photodiodes," J. Appl. Phys. **110**(2), 023107 (2011).
15. A. Rogalski, J. Antoszewski, and L. Faraone, "Third-generation infrared photodetector arrays," J. Appl. Phys. **105**(9), 091101 (2009).
16. M. N. Abedin, T. F. Refaat, I. B. Bhat, Y. Xiao, and D. G. Johnson, "Bias-selective operation of Sb-based two-color photodetectors," Proc. SPIE **6297**, 629709 (2006).
17. K. Swaminathan, T. J. Grassman, L. M. Yang, Q. Gu, M. J. Mills, and S. A. Ringel, "Optically-aligned visible/near-infrared dual-band photodetector materials and devices on GaAs using metamorphic epitaxy," J. Appl. Phys. **110**(6), 063109 (2011).
18. E. H. Steenbergen, M. J. Dinezza, W. H. G. Dettlaff, S. H. Lim, and Y. H. Zhang, "Optically-addressed two-terminal multicolor photodetector," Appl. Phys. Lett. **97**(16), 161111 (2010).

Optics EXPRESS

19. G. Masini, L. Colace, F. Galluzzi, G. Assanto, T. P. Pearsall, and H. Presting, "Voltage tunable SiGe photodetector: A novel tool for crypted optical communications through wavelength mixing," Appl. Phys. Lett. **70**(24), 3194–3196 (1997).
20. J. D. Hwang and K. H. Hseih, "Voltage-tunable dual-band infrared photodetectors with Si/SiGe metal-semiconductor-metal heterostructure," Microelectron. Eng. **85**(11), 2266–2268 (2008).
21. J. C. Campbell, T. P. Lee, A. G. Dentai, and C. A. Burrus, "Dual-wavelength demultiplexing InGaAsP photodiode," Appl. Phys. Lett. **34**(6), 401–402 (1979).
22. L. Colace, G. Masini, and G. Assanto, "Solid state wavemeter with InGaAsP/InGaAs two-diode heterostructure," Electron. Lett. **38**(14), 735–737 (2002).
23. E. R. Blazejewski, J. M. Arias, G. M. Williams, W. McLevige, M. Zandian, and J. Pasko, "Bias switchable dualband HgCdTe infrared photodetector," J. Vac. Sci. Technol. B **10**(4), 1626–1632 (1992).
24. J. A. Wilson, E. A. Patten, G. R. Chapman, K. Kosai, B. Baumgratz, P. Goetz, S. Tighe, R. Risser, R. Herald, W. A. Radford, T. Tung, and W. A. Terre, "Integrated two-color detection for advanced focal plane array (FPA) applications," Proc. SPIE **2274**, 117–125 (1994).
25. C. Rosenblad, H. R. Deller, A. Dommann, T. Meyer, P. Schroeter, and H. von Känel, "Silicon epitaxy by low-energy plasma enhanced chemical vapor deposition," J. Vac. Sci. Technol. A **16**(5), 2785–2790 (1998).
26. https://www.nextnano.de/
27. J. T. Teherani, W. Chern, D. A. Antoniadis, J. L. Hoyt, L. Ruiz, C. D. Poweleit, and J. Menéndez, "Extraction of large valence-band energy offsets and comparison to theoretical values for strained-Si/strained-Ge type-II heterostructures on relaxed SiGe substrates," Phys. Rev. B Condens. Matter Mater. Phys. **85**(20), 205308 (2012).
28. G. Isella, J. Osmond, M. Kummer, R. Kaufmann, and H. Känel, "Heterojunction photodiodes fabricated from Ge/Si (100) layers grown by low-energy plasma-enhanced CVD," Semicond. Sci. Technol. **22**(1), S26–S28 (2007).
29. G. Capellini, M. De Seta, P. Zaumseil, G. Kozlowski, and T. Schroeder, "High temperature x ray diffraction measurements on Ge/Si(001) heterostructures: A study on the residual tensile strain," J. Appl. Phys. **111**(7), 73518 (2012).
30. G. Zhou, K. H. Lee, D. H. Anjum, Q. Zhang, X. Zhang, C. S. Tan, and G. Xia, "Impacts of doping on epitaxial germanium thin film quality and Si-Ge interdiffusion," Opt. Mater. Express **8**(5), 1117–1131 (2018).
31. J. M. Hartmann, A. Abbadie, J. P. Barnes, J. M. Fédéli, T. Billon, and L. Vivien, "Impact of the H2 anneal on the structural and optical properties of thin and thick Ge layers on Si; Low temperature surface passivation of Ge by Si," J. Cryst. Growth **312**(4), 532–541 (2010).
32. F. Cai, Y. Dong, Y. Heng Tan, C. Seng Tan, and G. (Maggie) Xia, "Enhanced Si–Ge interdiffusion in high phosphorus-doped germanium on silicon," Semicond. Sci. Technol. **30**(10), 105008 (2015).
33. L. Colace, P. Ferrara, G. Assanto, D. Fulgoni, and L. Nash, "Low Dark-Current Germanium-on-Silicon Near-Infrared Detectors," IEEE Photonics Technol. Lett. **19**(22), 1813–1815 (2007).
34. J. Osmond, G. Isella, D. Chrastina, R. Kaufmann, M. Acciarri, and H. von Känel, "Ultralow dark current Ge/Si(100) photodiodes with low thermal budget," Appl. Phys. Lett. **94**(20), 201106 (2009).
35. L. Colace and G. Assanto, "Germanium on silicon for near-infrared light sensing," IEEE Photonics J. **1**(2), 69–79 (2009).

151.20.187.225 {ts '2019-03-08 10:56:17'}